

## Effect of airfoil distance to water surface on static stall

Y. Azarگون<sup>1</sup>, M. H. Djavareshkian<sup>1\*</sup>, E. Esmailifar<sup>1</sup>

<sup>1</sup>Department of Mechanical Engineering, Ferdowsi University of Mashhad, Iran. Phone: +989151095791

**ABSTRACT** – In this study, viscous, turbulent, and steady flow around an airfoil near the water surface has been simulated through a numerical method. In this simulation, Navier-Stokes equations have been solved using the finite volume method with a discretized second-order accuracy and PIMPLE algorithm. The Volume of Fraction (VOF) method has been employed to predict the free surface flow. A part of the simulation results has been validated through numerical and experimental data. Besides considering the style of flow separation in the angles of numerous attacks and airfoil static stall near the surface of the water. For this purpose, the airfoil simulation has been processed airfoil in the 68,000 Reynolds number, angle of attack of 2.5 to 11 degree and different distances from the water surface ( $h/c = 0.5, 1, \infty$ ). In a larger angle of attacks, flow is initially separated from the leading edge of the surface, and then it attaches to the surface at a lower point. This reattachment leads to an increase in adverse pressure gradient and the formation of a larger separation in the downstream of the airfoil. The pressure gradient dramatically increases, and the flow gets separated from the upstream of the airfoil. Upon lowering distance from the surface, static stall takes place at a higher point and a lower angle of attack, respectively.

### ARTICLE HISTORY

Revised: 26<sup>th</sup> Aug 2019

Accepted: 21<sup>st</sup> Sept 2019

### KEYWORDS

*Water surface;  
separation;  
static stall;  
airfoil.*

## INTRODUCTION

Wing-in-Ground effects (WIGs) have been highly taken into account in recent years with two prominent features that differentiate them from other aeronautical means. The first feature is their aerodynamic shape, which shows a very high lift to drag coefficient when it moves, and when it approaches the surface, this coefficient is higher than the airframe of similar dimensions, flying at high altitude outside the ground effect. Another distinction is that they have a good dynamic equilibrium that occurs when flying at low altitudes near the surface. This phenomenon was reported by pilots with the flight of the first planes in the years before 1920 when they were flying near the sea level observed that flying would require less energy [1]. In many empirical and numerical studies on this phenomenon, the basis of the problem is the study of the ground effect on aerodynamic coefficients of a static airfoil near the surface. Rozhdestvensky [2,3] introduced a mathematical model for static airfoil in the vicinity of the surface and presented an overview of WIG devices and their history. Daichinet et al. (2007) examined the effect of free surface on the vortex of the airfoil tail. The results of this experimental study were that the movement of vortices under the airfoil was stopped in all cases. The study of secondary flows and vortices produced at the tip of the wing near the ground surface was carried out by Climent et al [4]. Djavareshkian et al. [5,6] also examined another effective parameter, the effect of airfoil camber on lift coefficient in the ground effect and concluded that the positive effect of camber on the lift coefficient occurs only at small angles of attacks. In another study, they investigated the effect of a smart and conventional flap close to the ground and angle of attack and the angle of the vane corresponding to the highest lift-to-drag ratio. Nikhil et al. [7] studied the impact of the angle of attack on the close-to-ground airfoil aerodynamic coefficients. Other related studies include the studies conducted by Qu et al. [8,9] on the effect of airfoil angle of attack in a steady state at different flight altitudes on the aerodynamic properties of the flat and wave ground, and also on the flow physics of 3-element airfoil in static and dynamic states. Qu et al also numerically investigated the effect of angle of attack and distance from surface on the aerodynamic coefficients and flow physics of a NACA 4412 airfoil at ground effect, results showed in low to moderate angles of attack, with reduced distance from the surface, the effective angle of attack decreased, at the high angle of attack, with reduced distance from the surface, a large region of separated flow occurred and at the negative angle of attack producing the negative lift [10].

A year later Rostami et al. [11] studied an accurate viscous–inviscid interacting method as an alternative method to computing heavy Navier–Stokes solution for utilizing in the surface effect zone, that was good accuracy for predicting the effect of surface proximity [11]. Gao et al. [12] researched the aerodynamics and flow physics of a typical transonic RAE2822 airfoil at different angles of attack searched. They observed that at low angles of attacks a steady shock on the lower surface of the airfoil, also at small airfoil distance from the surface, the small angle of attack and high Mach numbers exists a new coupling between the shock buffets on the lower and the upper surface of the airfoil [12]. Other related studies include the studies conducted by Wei He et al. [13] studied a numerical–theoretical of the steady massively separated flow around a NACA 4415 airfoil at a low Reynolds number and a high angle of attack near the wavy ground, this research provided new insight into the stability of airfoil–ground flow systems at a low Reynolds number and a high angle of attack [13,14].

In many studies, for the numerical study of the free surface effect on the aerodynamic characteristics of the airfoil, the viscous fluid is not considered, and it is considered to be a rigid surface for ease in the simulation of the free surface. The purpose of this study is investigation static stall of airfoil near the water surface. Different attack angles and distance from the surface have been investigated. Airfoil simulation is carried out at  $h/c = 0.5, 1, \infty$  and at the angle of attack of 2.5 to 11 degree.

## GOVERNING EQUATION

The governing equations for two-dimensional incompressible flow, including the equations of continuity and momentum, are given in Equations. (1), (2) and (3), respectively:

$$\partial u / \partial x + \partial v / \partial y = 0 \quad (1)$$

$$u \left( \partial u / \partial x \right) + v \left( \partial u / \partial y \right) = - \left( 1 / \rho \right) \left( \partial p / \partial x \right) + \nu \left( \partial^2 u / \partial x^2 + \partial^2 u / \partial y^2 \right) \quad (2)$$

$$u \left( \partial v / \partial x \right) + v \left( \partial v / \partial y \right) = - \left( 1 / \rho \right) \left( \partial p / \partial y \right) + \nu \left( \partial^2 v / \partial x^2 + \partial^2 v / \partial y^2 \right) \quad (3)$$

In the above equations  $u$ ,  $v$ ,  $p$ ,  $\rho$  and  $\nu$  have shown horizontal and vertical velocity, Pressure, density and viscosity respectively. To simulate the two-phase flow and capture the free surface between the water and air, the method of the volume of flow has been used. In this method, the volume of the fraction is defined and the corresponding scalar transfer Equation. (4) is solved, which results in the ratio of the Volume of Fraction (VOF) of each flow component for each cell at any given moment [15,16].

$$\partial F / \partial t + u \left( \partial F / \partial x \right) + v \left( \partial F / \partial y \right) = 0 \quad (4)$$

If the volume of flow is  $F = 0$ , the cell is filled with air and if  $F = 1$ , the cell is filled with water. Also, cells with values of  $0 < F < 1$  are cells that contain some water and some air ( $F$  is mass flux) [17-20].

## NUMERICAL MODELING

The computational domain used is shown in Figure 1. The subject of this study is an airfoil with a cross-section of NACA0012 with a chord length of  $C = 1$  at a distance of  $h$  from the free surface of the water. A uniform free flow passes through the airfoil with velocity  $U$  in the  $x$ -direction. The mesh used in this research is fully structured. To better capture the free surface flow, the grid near the free surface is orthogonal. The mesh quality drops sharply around the airfoil. As a result, the C-type mesh is used around the airfoil and the H-type mesh geometry is selected in the rest of the solution in order to maintain the mesh quality both around the airfoil and around the free surface (Figure 2).

The height of the first cell on the airfoil wall is considered such that it always be  $y^+ < 5$ . In this situation, the first cell is located in the sub-layer, where the flow can be considered to be laminar, and the tension imposed on the wall can be calculated using the tension relationship in terms of strain in the laminar flow. Mesh around the free surface has also been thinned out to capture the free surface accurately.

To simulate the flow, firstly, the governing equations on the flow are discrete by a finite volume method, and then solved by the PIMPLE Algorithm (The PIMPLE Algorithm is a combination of PISO and SIMPLE). To capture the free surface, the volume of the fraction of the fluid has been used. Transition terms are discriminated using a second-order plan with the bounded feature. Then, by applying the boundary condition, the pressure is internally interpolated at the fixed velocity inlet, and at the fixed pressure outlet, the velocity is extrapolated inside the solution range. On the upper and lower boundaries, a symmetry boundary condition was used. For the boundary of the airfoil, shear stresses are calculated using wall functions and applied in discrete equations.

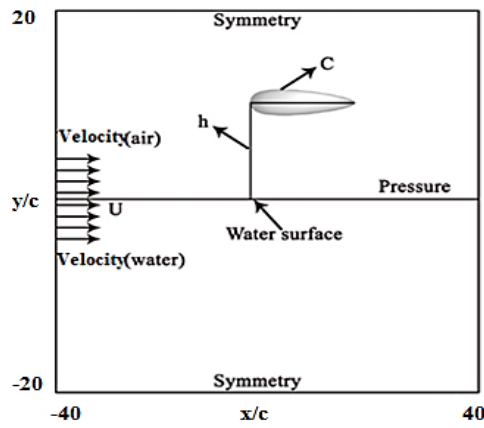


**Figure 1.** General schematic of problem and boundary condition.

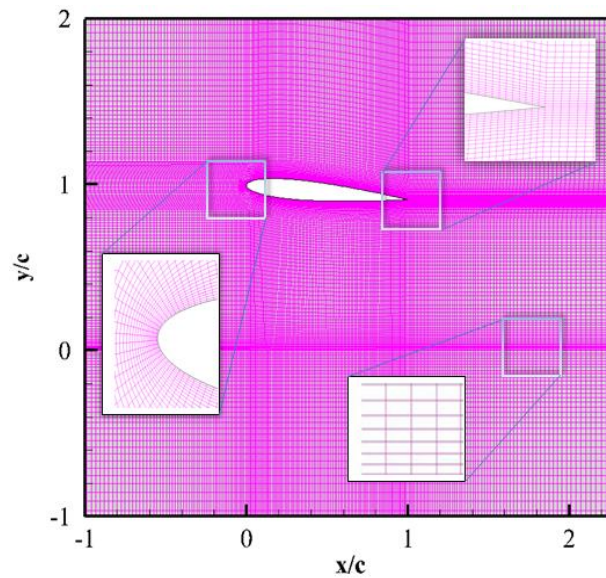


**Figure 2.** Mesh around airfoil and free surface.

To examine the independence of the results of the mesh, three different meshes with the same approach in the mesh were generated. The length of the mesh elements is reduced by a principled method with a constant ratio, i.e., the number of cells on all edges is increased by 1.2, and meshes with a population of 120,000, 170,000, and 200,000 cells were generated. The flow around the NACA0012 airfoil was solved for the three meshes. Figure 3 shows the distribution of the pressure coefficient in terms of location for the three different meshes. As it is seen, the distribution of the pressure coefficient for the mesh with 170,000 cells and the mesh with 200,000 cells are matching, so the independence of the mesh is achieved at the mesh with 170,000 cells.

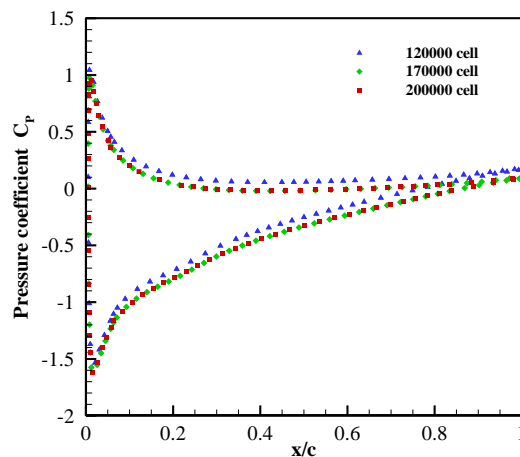


**Figure 3.** Mesh independency.

To validate, two simulations were carried out close to and far from the water surface and compared with the published results. For near-surface, the steady flows are simulated around an airfoil with an angle of attack of 5 degrees in  $h/c = 0.5, 1$  and the test conditions are used following Table 1, Results are compared with numerical data of reference [21] that are based on inviscid and non-rotating flow in Table 2.

**Table 1.** Geometric parameters and flow conditions of reference [21] for validation.

Variable	Value
Reynolds number	68000
Free flow velocity	1 m/s
Distance from surface (h/c)	0.5 and 1 of the chord length
Chord length	1 meter

**Table 2.** Value of lift coefficient at  $h/c = 0.5, 1$  and an angle of attack of 5 degrees.

Distance from surface	Reference [21]	The current simulation
$h/c = 0.5$	0.660781	0.519228
$h/c = 1$	0.581024	0.486619

The difference in the results of the two methods is that simulation has been carried out in the reference given with the assumption of the potential flow (non-rotational and inviscid flow), while in the present study, the Navier-Stokes equations are solved. For static stall validation, the results compared with published data of free flow, the flow around the NACA 634-021 airfoil at  $h/c = \infty$  is simulated under the same test conditions with reference [22]. The results are compared with the experimental data of this reference, the average error of results is % 4.47 and as Figure 4 shows, there are two acceptable matching curves indicate the correctness of the solution.

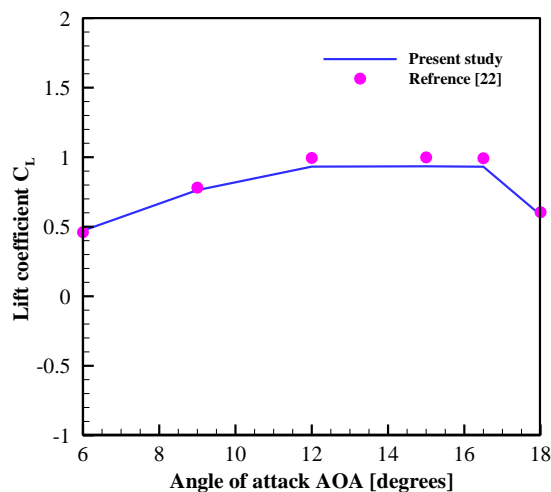


**Figure 4.** Validation static stall at  $h/c = \infty$ .

## RESULTS AND DISCUSSION

In this study, an airfoil near the water surface is simulated. The results presented for 3 different distances from the surface and for the range of the angle of attack of 2.5 to 11 degree were investigated to simulate the static stall phenomenon of airfoil near the water surface.

Figure 5 shows the variation of the lift coefficient in terms of the angle of attack at different flight altitudes. As can be seen, the maximum lift coefficient has increased with decreasing flight altitude; it is also observed that the value of the lift coefficient increases linearly with increasing angle of attack to an angle of about 8.5 degrees. Then, it sharply decreases with a plummeted slope, indicating the advance of separation to the leading edge and stall.

With increasing flight altitude, the angle of stall increase. At  $h/c = 1$  and an angle of attack of about 9.25 degrees, the lift coefficient is maximum, and then the amount of the lift coefficients slowly and then reduced at an angle of attack of 9.5 degree. In  $h/c = \infty$  the maximum value of the lift coefficient is at an angle of attack of 9.5 degrees, and after the angle

of attack of 10 degrees, the lift coefficient decreases sharply. As can be seen, there is a slight difference between the results at a distance of  $h/c = \infty$  and  $h/c = 1$  after the stall.

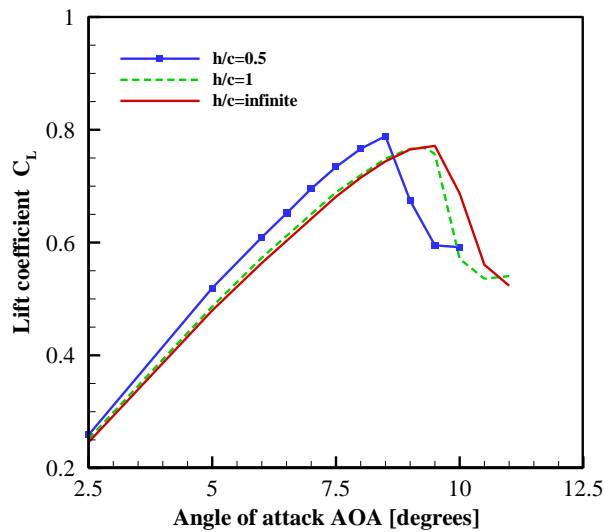


**Figure 5.** Lift coefficient at  $h/c = 0.5, 1, \infty$  and angle of attack of 2.5-11 degrees.

Figure 6 shows the variation of the drag coefficient in terms of the angle of attack at various flight altitudes. At an angle of attack = 5 degrees, the adverse pressure gradient is mild on the upper surface of the airfoil. As shown by the distribution of the pressure coefficient, the boundary layer is slowly attached from the edge of the attack to the edge of the airfoil surface and there is no flow separation. Therefore, the airfoil drag coefficient at a 5-degree attack angle is a small amount. As the angle of attack increases, the adverse pressure gradient that causes separation increases. Since the smooth boundary layer is not able to withstand adverse pressure gradient, it separates from the upper surface of the airfoil, and the separation of the flow occurs at the angle of attack of greater than 8.5 degrees. The slowly separated boundary layer is rapidly transferred to the turbulent flow and the vortex is produced. This turbulent flow, as a turbulent boundary layer, attaches to the trailing edge to the upper surface of the airfoil. The drag coefficient increases with an increase in the attack angle. At  $h/c = 0.5$  and angle of attacks 9, 9.5 and 10 degree, the adverse pressure gradient increases sharply on the surface of the airfoil, and the complete stall occurs, so the drag coefficient increases strongly and the lift coefficient decreases significantly. After the airfoil stall, with increasing angle of attack, the lift coefficient increases with a low velocity, and the drag coefficient increases rapidly. As shown in the graph of the drag coefficient, the stall angle has increased with increasing distance from the surface. It is also observed that in  $h/c = \infty$ , the variation of the drag coefficient in terms of the angle of attack and stall is less different from the previous state.

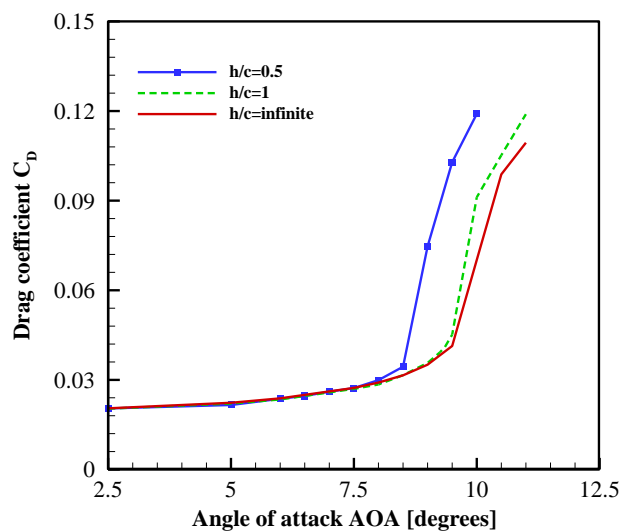


**Figure 6.** Drag coefficient at  $h/c = 0.5, 1, \infty$  and angle of attack of 2.5 to 11 degrees.

Figures 7(a-c), show the distribution of the pressure coefficient around the NACA0012 airfoil in different states. It can be seen that with lower flight altitude at a constant attack angle, the pressure at the lower airfoil level has increased. It is also observed that with increasing angle of attack, although the distribution of pressure on the lower surface of the

airfoil does not change significantly, the distribution of the pressure coefficient varies over the upper surface of the airfoil due to the change in the position of the stagnation point. When the angle of attack is small, (angle of attack = 5 degrees), there is no separation near the edge of the airfoil attack, and as the angle of attack increases, the position of the minimum point of pressure on the upper airfoil surface is lowered. At the larger angle of the attacks, the distribution of the pressure coefficient and the minimum point of pressure have increased on the upper surface of the airfoil due to static tall and the complete separation of the boundary layer.

In the graph of  $h/c = 1$  (Figure 7(a)), at the angle of about 8.5 degrees, the greatest difference in pressure was made at the upper and lower levels of the airfoil, the greatest difference was increased with increasing distance from the surface. As in  $h/c = 1$  (Figure 7(b)), the maximum pressure distribution interval is at the angle of attack of about 9.25 degree and in  $h/c = \infty$  (Figure 7(c)), at an angle of attack of 9.5 degrees. It can be seen that in all cases, after reaching the highest difference in pressure level between the upper and lower levels of the airfoil, the pressure distribution interval initially slowly and then dropped sharply, indicating the complete separation of flow and stall. It is also seen that with increasing distance from the surface, the effect of the water level on the surface below the airfoil is less and the results are closer to far from the surface state.

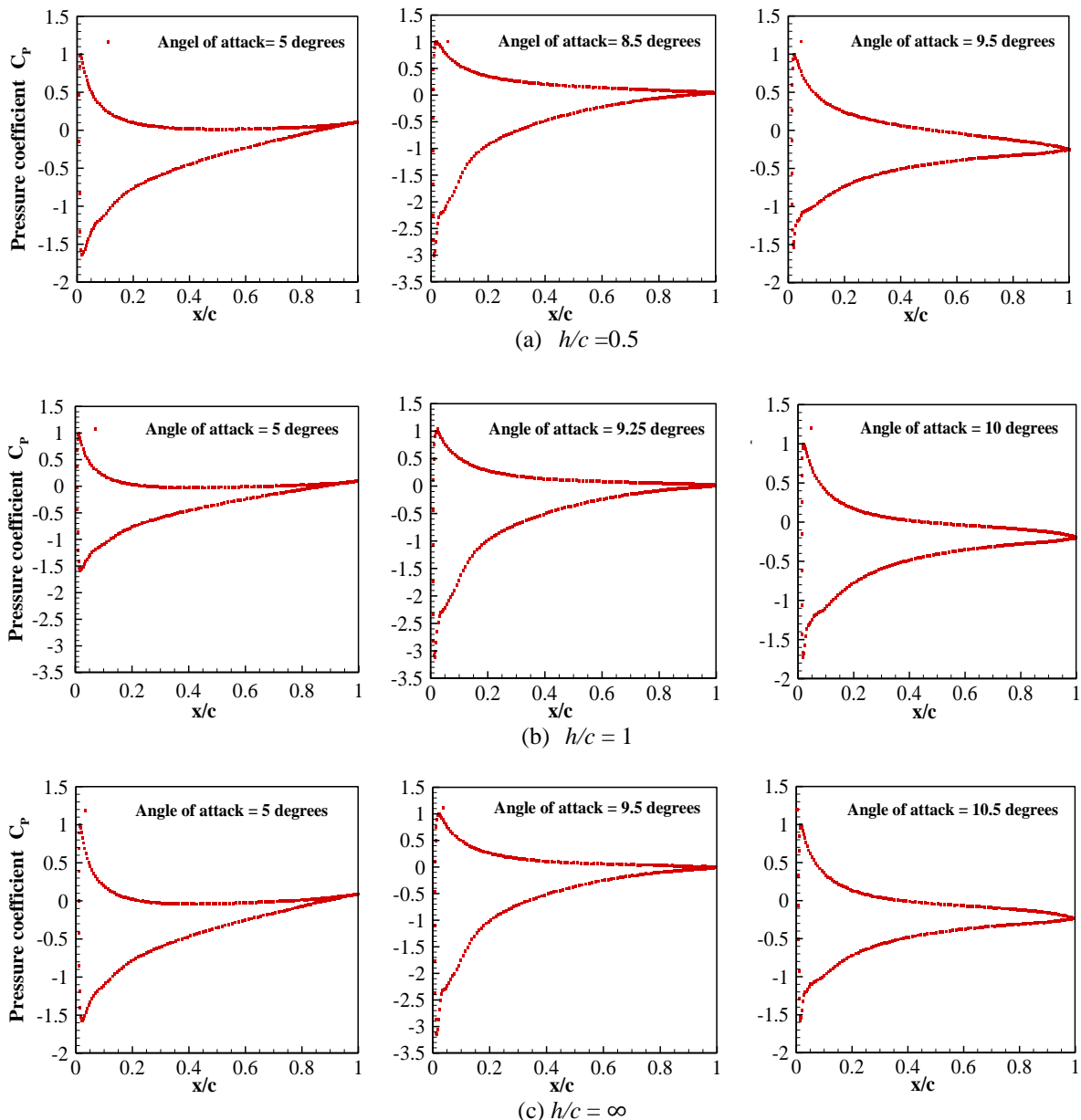


**Figure 7.** Pressure coefficient at different distance from surface and angle of attack (AOA).

Figure 8 shows the pressure contour with the streamlines at the angle of attack of 5 degrees, at  $h/c = 0.5, 1, \infty$ . It can be seen that with the decrease of altitude, the pressure in the duct between the surface below the airfoil and the surface of the water has increased. At the low angle of attack (5 degrees), the pressure gradient is mild, and the flow in the upper

and lower surface of the airfoil is fully attached to the surface and passes without any separation from the surface. At the bottom of the airflow, the adverse pressure gradient is increased and the flow is slightly separated from the surface.

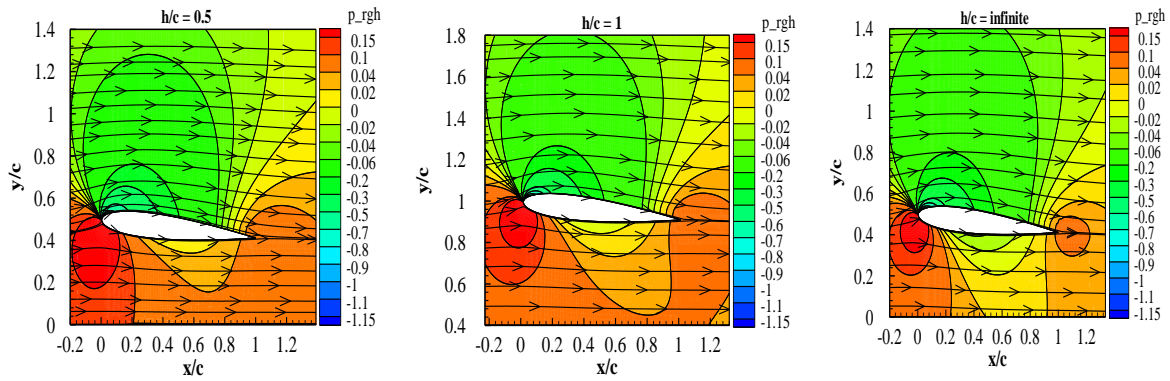


**Figure 8.** Pressure contour with streamline at different distance from surface ( $h/c$ ) and angle of attack = 5 degrees.

In Figure 9(a-c), it can be clearly seen that on the upper surface of the airfoil in the downstream, the position of  $x/c = 0.92$  (Figure 9(a)),  $x/c = 0.93$  (Figure 9(b)) and  $x/c = 0.939$  (Figure 9(c)) for the direction of the path is in the opposite direction of the mainstream. It is clear that by reducing the airfoil distance from the surface, the separation of the boundary layer has occurred a little earlier. As a result of this low return flow and the separation of the boundary layer, a very small vortex region is created at the bottom of the airfoil; the size of the vortex near the surface is slightly larger (Figure 10). This small vortex area, in all cases down the airfoil, causes a very low drag force on the airfoil, which is confirmed by drag coefficient in Figure 6.

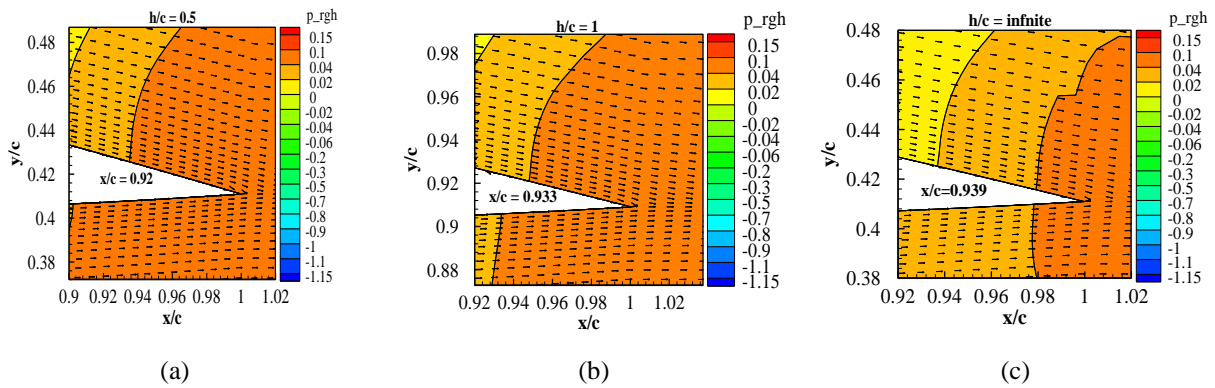


**Figure 9.** Vector in trailing edge at different distance from surface ( $h/c$ ) and angle of attack = 5 degrees.

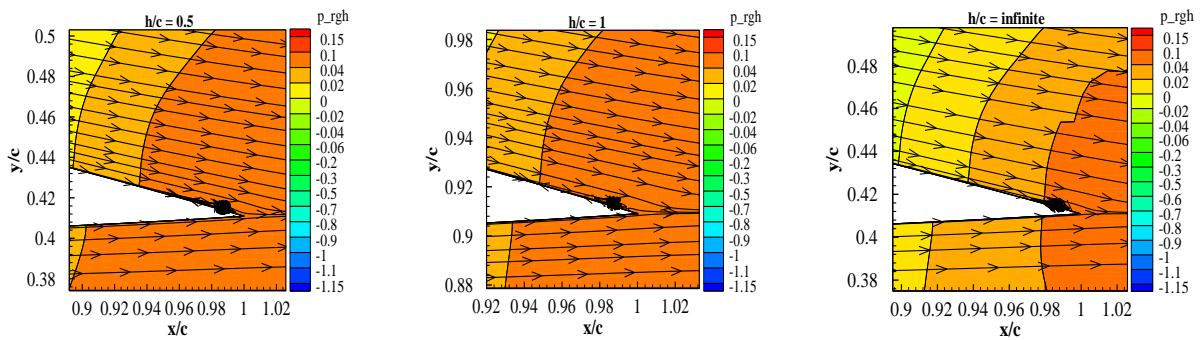


**Figure 10.** Vortex in trailing edge at different distance from surface ( $h/c$ ) and angle of attack = 5 degrees.

In Figures 5 and 6, the highest amount of aerodynamic coefficients was observed in  $h/c = 0.5, 1, \infty$  at the angle of attack = 8.5, 9.25 and 9.5 degrees respectively. Figure 11 shows the pressure contour along with the streamlines in terms of position 0.5 m distance from the surface in the attack angle of 8.5 degrees,  $h/c = 1$  at an angle of attack 9.25 degrees and  $h/c = \infty$  at an angle of attack of 9.5 degrees.

In all modes, the pressure on the upper surface of the airfoil is almost the same as the previous state (5 degrees), and is lower at the lower surface of the airfoil. The streamline sat the surface below the airfoil are approximately the same as the previous state and the flow is fully attached to the surface, but the behavior of the streamlines at the high level of the airfoil is different from the previous state.

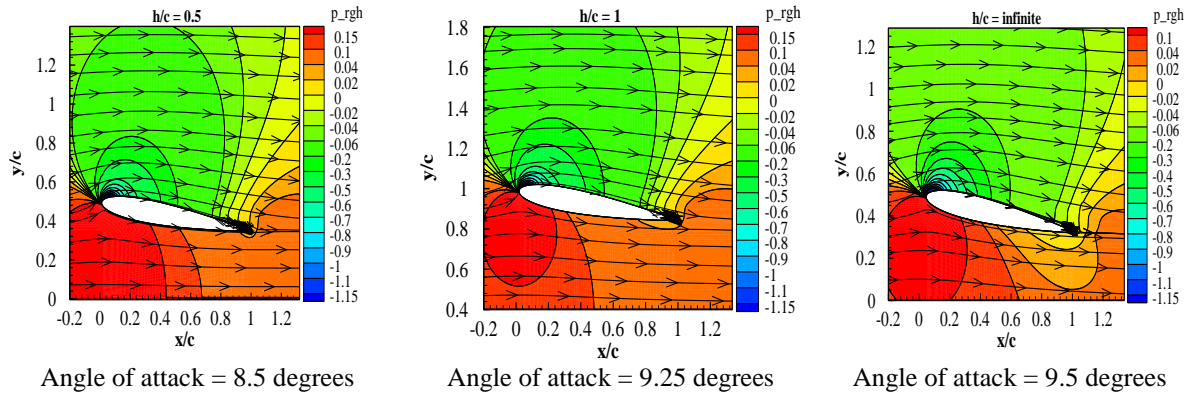


**Figure 11.** Pressure contour and streamline at angle of attack of  $CL_{MAX}$  for different distance from surface ( $h/c$ ).

Figure 12 shows the position of the separation point on the upper surface of the airfoil. As it is known, at the  $h/c = 0.5$  separation point is in the position  $x/c = 0.036$ , and the flow in the range of  $x/c = 0.036-0.130$  is separated from the surface. By increasing the distance from the surface, at  $h/c = 1$  and the angle of attack 9.25 degree, the separation point is  $x/c = 0.037$  and the flow separation continues to the point  $x/c = 0.130$ . At  $h/c = \infty$  at the point of  $x/c = 0.610$ , the separation of the flow has occurred, and the flow is separated from the upper surface to the position of  $x/c = 0.121$ . Due to the increase of pressure distribution, the slowly separated boundary layer attaches to the turbulent flow, which causes the reattachment of separated boundary layer to the upper surface of the airfoil at the points of  $x/c = 0.122, 0.138, 0.130$  (at  $h/c = 0.5, 1, \infty$  respectively) as the turbulent boundary layer. This flow is called a secondary flow. The separation of the flow causes a small vortex in the above areas (shown in Figure 13).

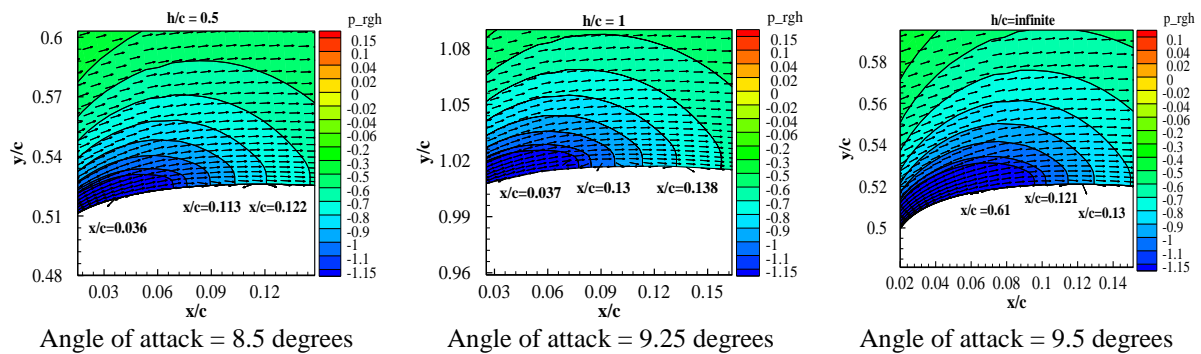


**Figure 12.** Initial separation of flow and flow reattachment at  $CL_{max}$  angle of attack and at different distance from surface ( $h/c$ ).

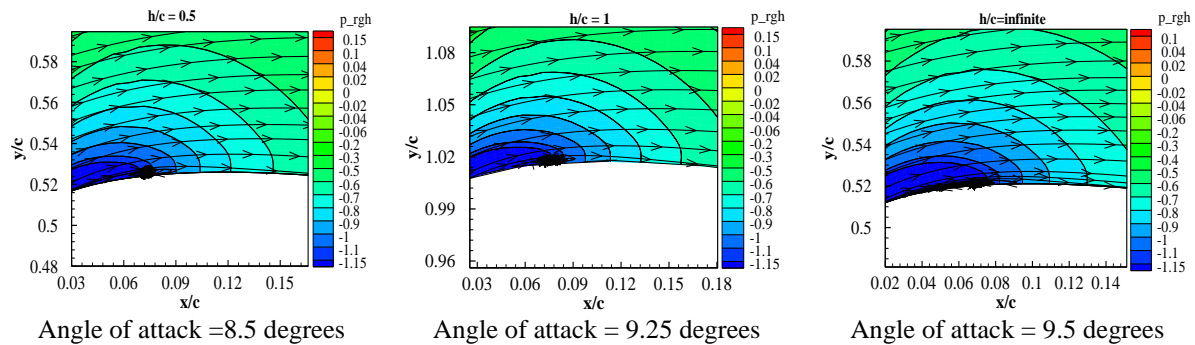


**Figure 13.** Vortex in the initial separation of flow at  $CL_{max}$  angle of attack and at different distance from surface ( $h/c$ ).

The turbulent boundary layer has a greater amount of energy to counteract the adverse pressure gradient than the smooth boundary layer and is later separated from the surface. Therefore, after reattachment, the turbulent boundary layer remains up to the  $x/c = 0.625, 0.570, 0.545$  positions (Figure 14). The same flow reattachment has significantly increased the adverse pressure gradient and the re-separation flow.

Figure 15 shows that, in all modes, more path lines have deviated from the main direction of the flow and more separation area is formed at the bottom of the airfoil compared to the 5 degrees angle. It is seen in Figure 16 that the vortex flow region at the bottom of the airfoil has also grown and a larger vortex region has been created. As a result, the created drag force on the airfoil is more than the previous one (angle of attack of 5 degrees).

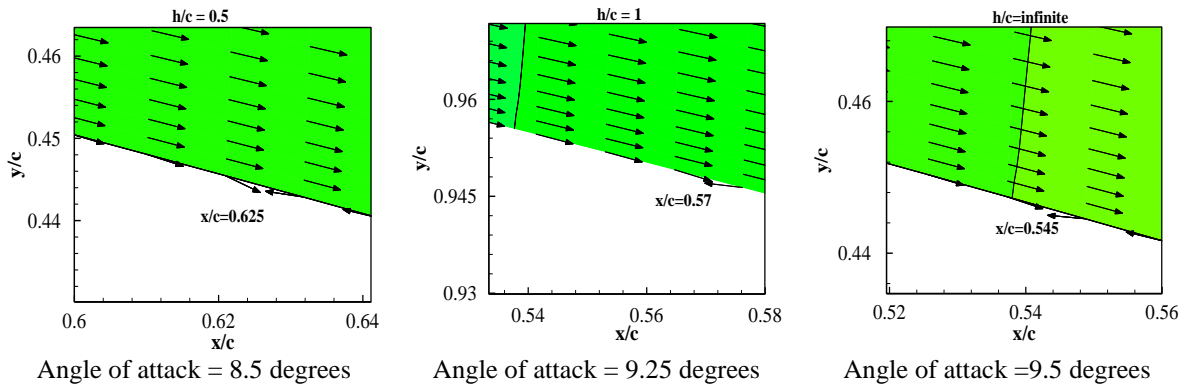


Figure 14. The last point of flow attachment at  $CL_{max}$  angle of attack and different distance from surface ( $h/c$ ).

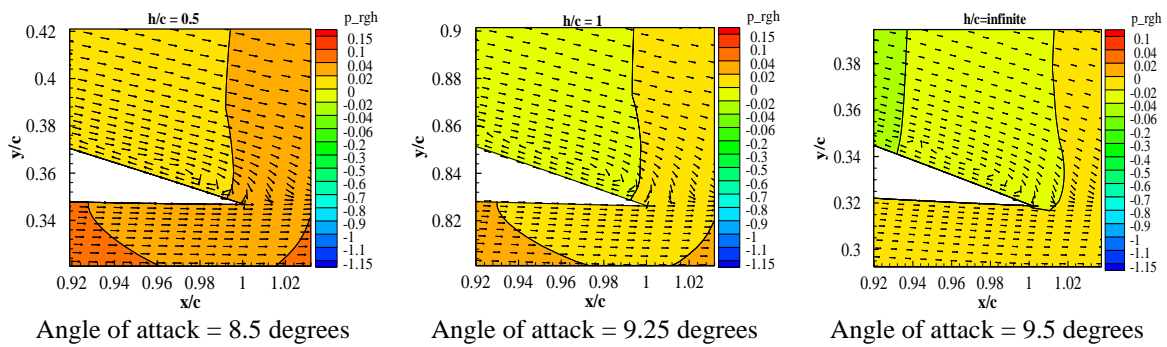


Figure 15. Path lines of the second flow separation path at the trailing edge at  $CL_{max}$  angle of attack and different distance from surface ( $h/c$ ).

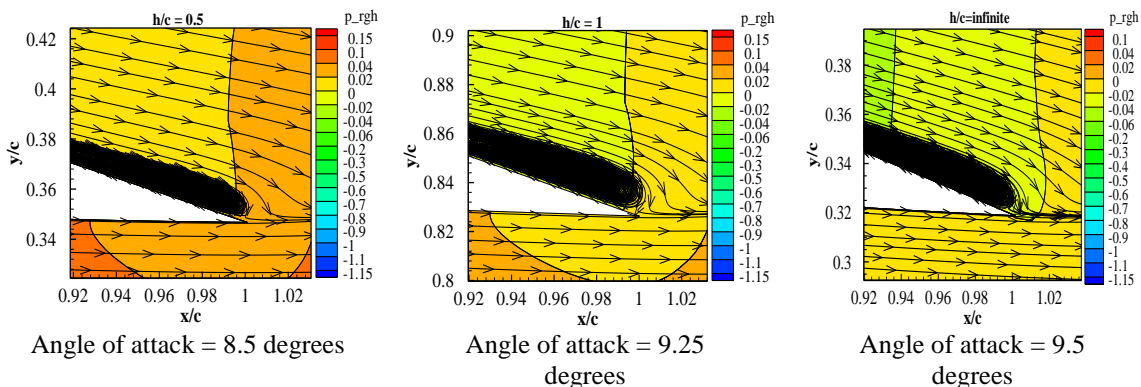


Figure 16. Vortex in the second flow separation at the trailing edge at  $CL_{max}$  angle of attack and different distance from surface ( $h/c$ ).

Figure 17 shows the pressure contour and the streamlines for  $h/c$  of 0.5, 1 and  $\infty$ , respectively, at the angle of attack of 9.5, 10 and 10.5 degrees. At all distances, the minimum point of the pressure distribution is reduced and the adverse pressure gradient at the high level of the airfoil is very intense, in this case, the separated layer cannot reattach to the surface. As the behavior of the streamlines in the pressure contours is shown in Figure 17, the flow is completely separated

from the edge of the attack to the edge of the trailing with a large separation angle from the upper surface of the airfoil and due to the sharp drop in the lift coefficient (Figure 6), there has been a complete stall at these angles.

The large separation of the flow has created a large area of recursive flow (Figure 18) and vortex flow (Figure 19) on the upper surface of the airfoil, and this area has greatly increased at the bottom of the airfoil. Figure 19 shows that the vortices of the trailing edge near the surface are larger and, as shown in Figure 6, these returning and vortex flows have caused a significant increase in the airfoil drag coefficient. It can be seen from the comparison of Figure 11 at  $h/c = \infty$  and Figure 17 at  $h/c = 0.5$  that flow has a different behavior at the same angle of attack at two distances from the surface. In Figure 11, which corresponds to  $h/c = \infty$  the secondary flow caused by the reattachment of flow to the surface has been created and, according to Figure 5, the maximum lift coefficient has been created, while, in Figure 17 ( $h/c = 0.5$ ), a severe gradient of the adverse pressure was created and flow could not attach to the surface and was separated from the surface at the very beginning of the leading edge. Also, the lift coefficient has dropped sharply and the complete stall has occurred.

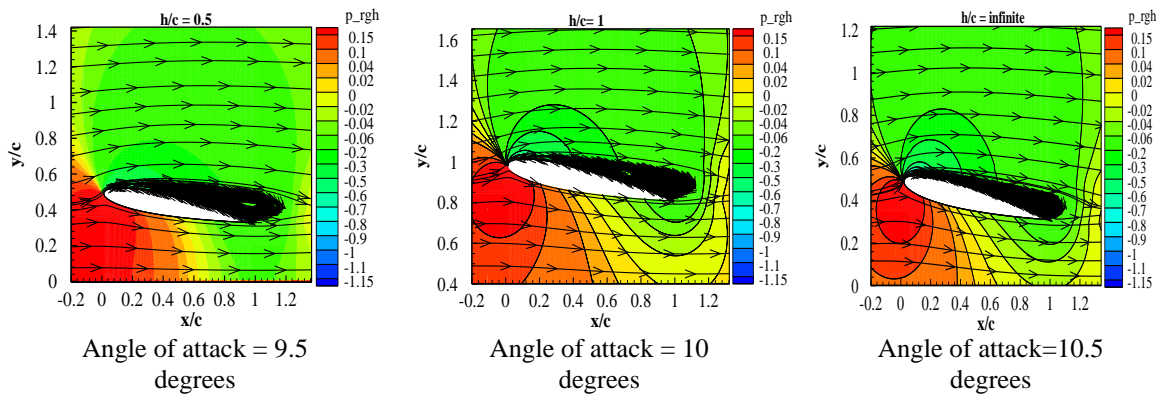


Figure 17. Pressure Contour and leading edge after static stall at different distance from surface ( $h/c$ ).

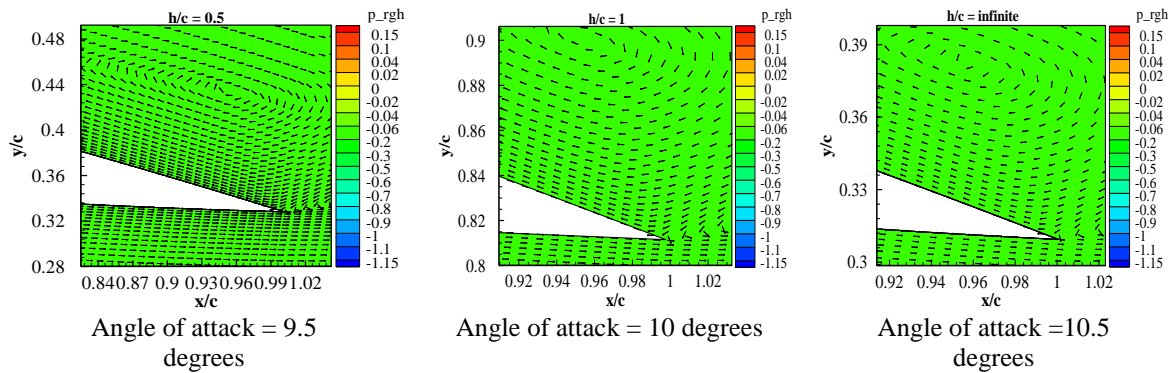


Figure 18. Path lines at trailing edge after static stall at different distance from surface ( $h/c$ ).

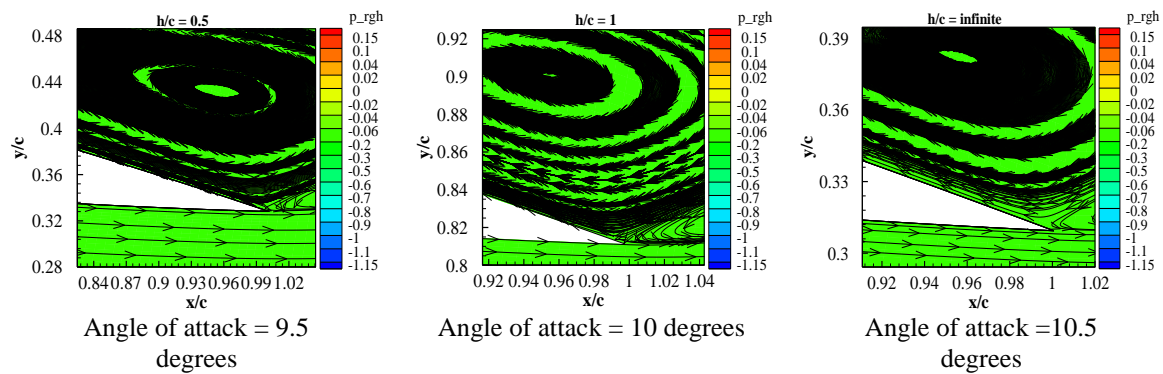


Figure 19. Vortex at the trailing edge after static stall at different distance from surface ( $h/c$ ).

## CONCLUSION

In this study, the effect of free surface on the separation of flow and static stall of a NACA0012 airfoil in the 68,000 Reynolds number at the angle of attack of 2.5 to 11 degrees at  $h/c = 0.5, 1, \infty$  distances from the water surface has been investigated. In the present numerical study, taking into account the effect of viscosity and the effect of free flexible surface, two-phase flow is defined using the volume of flow and Navier-Stokes equations have been solved using a two-phase flow solver.

The results show that the separation of flow from the surface depends on adverse pressure gradient strength. The adverse gradient is small at low angles, and the separation of flow occurs only in the small part at the bottom of the airfoil. As the angle of attack increases, the power of the adverse gradient increases, in this case, the flow is first separated from the surface near the leading edge. By increasing the flow pressure in the laminar boundary layer, it is connected to the turbulent boundary layer, and it again attaches to the surface. The turbulent boundary layer is of more energy than the laminar boundary layer, it is more resistant to separation and adverse pressure gradient and remains attached to the surface close to the trailing edge. Then, adverse pressure loses its energy by increasing the gradient and becomes separated from the surface. In this case, the intensity of the separation is greater than the low attack angle (5 degrees), more return and vortices flow are created at the trailing edge.

At the larger angle of attacks, the gradient of the adverse pressure is very intense, and the flow lacks the required energy to counter this adverse pressure gradient. The flow is separated from the surface from the beginning of the edge of the attack, and static stall occurs. At a distance from different surfaces and common attack angles, flow behavior is different, with distance from the surface, even at low attack angles, the separation of flow occurs at a higher point (closer to the leading edge). At the higher attack angle, the flow near the surface has completely be separated from the surface, stall occurs, and the lift coefficient has fallen sharply, while away from the surface, at this common angle, the secondary flow is generated and the highest value of lift coefficient is created, so that the complete separation of the flow and static stall occur sooner when the airfoil is near the surface.

## REFERENCES

- [1] Wieselsberger C. Wing resistance near the ground. National Advisory Committee for Aeronautics. 1922.
- [2] Rozhdestvensky KV. Matched asymptotics in aerodynamics of WIG vehicles. Proc. Intersociety High Performance Marine Vehicle and Exhibit HMP 92. 1992:17-27, June 24-27.
- [3] Rozhdestvensky KV. Wing-in-ground effect vehicles. Progress in Aerospace Sciences. 2006; 42(3): 211-283.
- [4] Daichin, Kang W, Zhao L. PIV measurements of the near-wake flow of an airfoil above a free surface. Journal of Hydrodynamics. 2007; 19(4): 482-487.
- [5] Djavareshkian MH, Esmaeli A, Parsania A. A comparison of smart and conventional flaps close to ground on aerodynamic performance. Journal of Aerospace Science and Technology. 2010; 7(2): 121-134.
- [6] Djavareshkian MH, Esmaeli A, Parsani A. Aerodynamics of smart flap under ground effect. Aerospace Science and Technology. 2011;15:642-652.
- [7] Pillai NS, Anil T, Aravind R, Vinod R, Kumar SE, Zaid ZU, Antony J, Manojkumar M. Investigation on airfoil operating in Ground Effect region. International Journal of Engineering & Technology. 2014; 3: 540.
- [8] Qu Q, Ju B, Huang L, Liu P, Agarwal RK. Flow physics of a multi-element airfoil in ground effect. In 54<sup>th</sup> AIAA Aerospace Sciences Meeting. 2016.
- [9] Qu Q, Lu Z, Liu P, Agarwal RK. Numerical study of aerodynamics of a wing-in-ground-effect craft. Journal of Aircraft. 2014; 51: 913-924.
- [10] Qu Q, Wang W, Liu P, Agarwal RK. Airfoil aerodynamics in ground effect for wide range of angles of attack. AIAA Journal. 2015; 53: 1048-1061.
- [11] Rostami A B, Ghadimi P, Ghasemi H. Adaptive viscous–inviscid interaction method for analysis of airfoils in ground effect. Journal of the Brazilian Society of Mechanical Sciences and Engineering. 2016; 38: 1593-1607.
- [12] Gao B, Qu Q, Agarwal RK, Aerodynamics of a transonic airfoil in ground effect. In 35<sup>th</sup> AIAA Applied Aerodynamics Conference. 2017.
- [13] He W, Guan Y, Theofilis V, Li LKB. Stability of low-reynolds-number separated flow around an airfoil near a wavy ground. AIAA Journal. 2019; 57: 29-34.
- [14] He W, Pérez JM, Yu P, Li LKB. Non-modal stability analysis of low-Re separated flow around a NACA 4415 airfoil in ground effect. Aerospace Science and Technology. 2019; 92: 269-279.
- [15] Esmailifar E, Djavareshkian MH, Feshalami BF, Esmaeli A. Hydrodynamic simulation of an oscillating hydrofoil near free surface in critical unsteady parameter. Ocean Engineering. 2017; 141: 227-236.
- [16] Menter FR. Two-equation eddy-viscosity turbulence models for engineering applications. AIAA Journal. 1994; 32: 1598-1605.
- [17] Tran M, Memon Z, Saieed A, Pao W, Hashim F. Numerical simulation of two-phase separation in T-junction with experimental validation. Journal of Mechanical Engineering and Sciences. 2018; 12: 4216-4230.
- [18] Memon Z, Pao W, Hashim F, Ahmed S. Experimental investigation of multiphase separation in different flow regimes through T-junction with an expander section. Journal of Mechanical Engineering and Sciences. 2019; 13: 5163 - 5181.

- [19] Saeid NH. Numerical predictions of sand erosion in a choke valve. *Journal of Mechanical Engineering and Sciences*. 2018; 12: 3988-4000.
- [20] Saieed A, Sam B, Pao W, Hashim FM. Numerical investigation of side arm gas volume fraction in two phase T-junction. *Journal of Mechanical Engineering and Sciences*. 2016; 10: 2311-2323.
- [21] Liang H, Wang X, Zou L, Zong Z. Numerical study of two-dimensional heaving airfoils in ground effect. *Journal of Fluids and Structures*. 2014; 48: 188-202.
- [22] Custodio D, Henochoa C, Johari H. Aerodynamic characteristics of finite span wings with leading-edge protuberances. *AIAA Journal*. 2015; 53: 1878-1893.